Global surface slopes and roughness of the Moon from the Lunar Orbiter Laser Altimeter

M. A. Rosenburg,[1] O. Aharonson,[1] J. W. Head,[2] M. A. Kreslavsky,[3] E. Mazarico,[4,5] G. A. Neumann,[4,5] D. E. Smith,[4,5] M. H. Torrence,[5] and M. T. Zuber[4,5]

Received 23 August 2010; revised 3 November 2010; accepted 15 November 2010; published 3 February 2011.

[1] The acquisition of new global elevation data from the Lunar Orbiter Laser Altimeter, carried on the Lunar Reconnaissance Orbiter, permits quantification of the surface roughness properties of the Moon at unprecedented scales and resolution. We map lunar surface roughness using a range of parameters: median absolute slope, both directional (along-track) and bidirectional (in two dimensions); median differential slope; and Hurst exponent, over baselines ranging from ~17 m to ~2.7 km. We find that the lunar highlands and the mare plains show vastly different roughness properties, with subtler variations within mare and highlands. Most of the surface exhibits fractal-like behavior, with a single or two different Hurst exponents over the given baseline range; when a transition exists, it typically occurs near the 1 km baseline, indicating a significant characteristic spatial scale for competing surface processes. The Hurst exponent is high within the lunar highlands, with a median value of 0.95, and lower in the maria (with a median value of 0.76). The median differential slope is a powerful tool for discriminating between roughness units and is useful in characterizing, among other things, the ejecta surrounding large basins, particularly Orientale, as well as the ray systems surrounding young, Copernican-age craters. In addition, it allows a quantitative exploration on mare surfaces of the evolution of surface roughness with age.

Citation: Rosenburg, M. A., O. Aharonson, J. W. Head, M. A. Kreslavsky, E. Mazarico, G. A. Neumann, D. E. Smith, M. H. Torrence, and M. T. Zuber (2011), Global surface slopes and roughness of the Moon from the Lunar Orbiter Laser Altimeter, *J. Geophys. Res.*, *116*, E02001, doi:10.1029/2010JE003716.

1. Introduction

[2] As signatures of surface evolution processes acting over geologic time, surface slopes and slope distributions provide important clues to the morphologic history of a planetary surface in terms of both formation and modification mechanisms. Moreover, the comparison of surface regions based on quantitative measures of roughness and its scale dependence is a powerful tool for interpreting the relationships between geologic and topographic units and their origins and has been successfully employed for various planetary bodies, including Earth [e.g., *Morris et al.*, 2008; *Neumann and Forsyth*, 1995; *Smith and Jordan*, 1988], Mars [e.g., *Aharonson et al.*, 2001; *Orosei et al.*, 2003; *Kreslavsky and Head*, 2000], and Venus [e.g., *Sharpton and Head*, 1985]. Attempts to study surface roughness on the Moon have spanned the decades between the Apollo era and the present [*Daniels*, 1963; *Moore and Tyler*, 1973; *Yokota et al.*, 2008], yet to date no comprehensive study of surface slopes and slope distributions has been possible at high resolution and across many scales.

[3] The Lunar Orbiter Laser Altimeter (LOLA) began collecting data in late June 2009, after the successful entry into orbit of the Lunar Reconnaissance Orbiter (LRO) [*Smith et al.*, 2010a; *Zuber et al.*, 2010]. With a ground track configuration consisting of five illuminated spots on the surface arranged in a cross pattern (Figure 1), LOLA allows for determination of slopes at multiple baselines, both between pairs of spots within each laser shot and between sequential shots. The high vertical precision (10 cm), accuracy (~1 m), and high density (~57 m along-track spacing) of LOLA measurements permit an unprecedented opportunity for quantitative morphologic characterization of the lunar surface relevant to current and past surface processes as well as to future lunar landing site selection. For comparison, the Mars Orbital Laser Altimiter operated with a vertical precision of ~1.5 m, a spatial accuracy of ~100 m (including pointing errors), and an along-track spacing of ~300 m [*Smith et al.*, 2001].

2. Topography Data

[4] LRO maintains a nearly circular, 50 km polar orbit that scans all longitudes of the Moon each month. We use

[1]Division of Geological and Planetary Sciences, California Institute of Technology, Pasadena, California, USA.
[2]Department of Geological Sciences, Brown University, Providence, Rhode Island, USA.
[3]Department of Earth and Planetary Sciences, University of California, Santa Cruz, California, USA.
[4]Department of Earth, Atmospheric, and Planetary Science, Massachusetts Institute of Technology, Cambridge, Massachusetts, USA.
[5]NASA Goddard Space Flight Center, Greenbelt, Maryland, USA.

Copyright 2011 by the American Geophysical Union.
0148-0227/11/2010JE003716

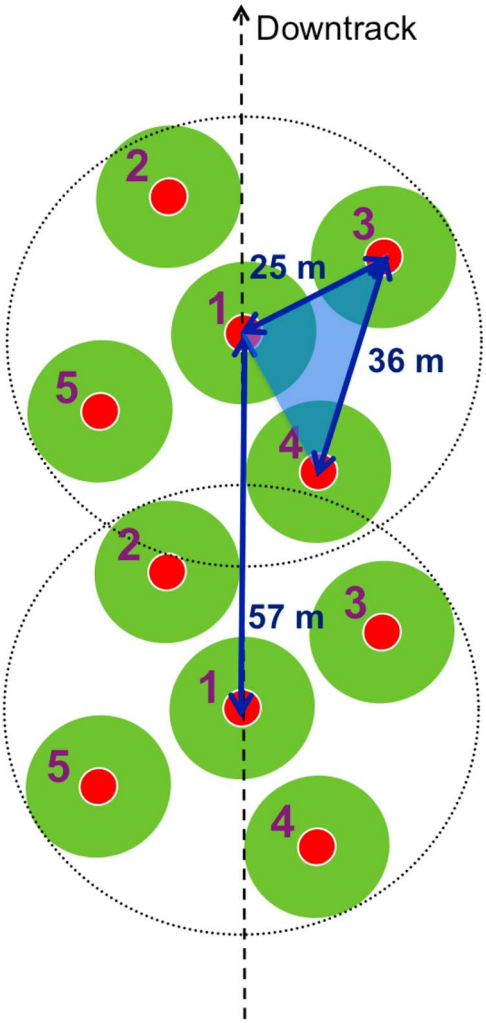

Figure 1. Plan view of two consecutive LOLA shots with spot numbers labeled. The shot-to-shot distance is ~57 m, and the smallest point-to-point baseline available is ~25 m. An example of a triangle used to calculate bidirectional slopes is shaded in blue. Red circles indicate the illuminated footprint of each laser spot, while green circles represent the field of view of each detector.

3180 tracks from the commissioning and mapping mission phases, acquired from 17 September 2009 to 9 March 2010, to compute and analyze a variety of parameters describing surface slopes and roughness. The data were processed to remove anomalous points (due to instrumental effects such as noise) and are spaced ~57 m apart along track and on average ~3.8 km across track at the equator and closer at the poles. Additional data have narrowed the cross-track spacing to ~1.8 km at the equator [*Smith et al.*, 2010b].

3. Global Surface Roughness of the Moon

[5] Quantitative measures of surface roughness have been defined in the literature in a number of ways. Here we investigate several measures of surface roughness, both in the interest of robustness in characterizing roughness units and to facilitate comparison with the literature. For one-dimensional slopes, we examine the RMS slope, the median absolute slope, and the median differential slope for a variety of horizontal scales, as well as the Hurst exponent, which describes how slopes scale with baseline (where the baseline is the horizontal length scale over which the slope is measured). In addition, LOLA's five-spot pattern allows for the calculation of two-dimensional slopes by fitting a plane to a set of three points along the track, resulting in the magnitude and direction of steepest descent.

3.1. RMS and Median Slopes

[6] The RMS slope is routinely calculated for the statistical analysis of topography because radar reflection scatter is often parameterized with this metric. In one dimension, it is defined as the RMS difference in height, Δz, between each pair of points (also known as the deviation, ν) divided by the distance between them, Δx:

$$s(\Delta x) = \frac{\nu(\Delta x)}{\Delta x} = \frac{1}{\Delta x}\left\langle [z(x_i) - z(x_{i-1})]^2 \right\rangle^{\frac{1}{2}}, \qquad (1)$$

where the angle brackets indicate the mean. However, because the RMS slope depends on the square of the deviation, this parameter is quite sensitive to outliers; this poses a significant problem because the slope-frequency distribution for natural surfaces is often non-Gaussian with strong tails. The median absolute slope is a more robust measure of typical slopes, as it is less affected by long tails in the distribution.

[7] To find the RMS and median slope in the along-track direction, point-to-point slopes were calculated for each track, stored at the midpoint, and averaged according to (1) within 0.5° (~15 km) sliding windows, each spaced 0.25° (~7.5 km) apart. The LOLA lasers have a firing frequency of 28 Hz, corresponding to a shot density of approximately 540 shots per degree down track, or roughly 270 shots per window at best. However, owing to noise and instrument performance issues, missing points are not uncommon. Since the RMS slope is sensitive to the number of points, N, included in each window, uneven N across the surface can introduce variations in the RMS slope map that are not due to real roughness features. To minimize this bias, windows were only considered valid if more than 250 measurements contributed to the average in that location. The median absolute (unsigned) slope is far less sensitive to the number of points in each bin. Given LOLA's ground spot pattern, the smallest baseline available for slope calculations is about 25 m, the distance on the surface from the center spot to any of the four corners (Figure 1).

[8] One-dimensional slopes calculated along profile underestimate the true gradient of the surface wherever the direction of steepest descent diverges from the along-track direction. At the smallest scales, this ambiguity can be resolved by computing the slopes in two dimensions from multiple points within each laser shot. We use vector geometry to compute the plane passing through three spots, recording the magnitude and azimuth of the slope. One such triangle appears as a shaded region in Figure 1. The effective baseline of the slope is taken to be the square root of the area of the triangle. The slope values are then binned as

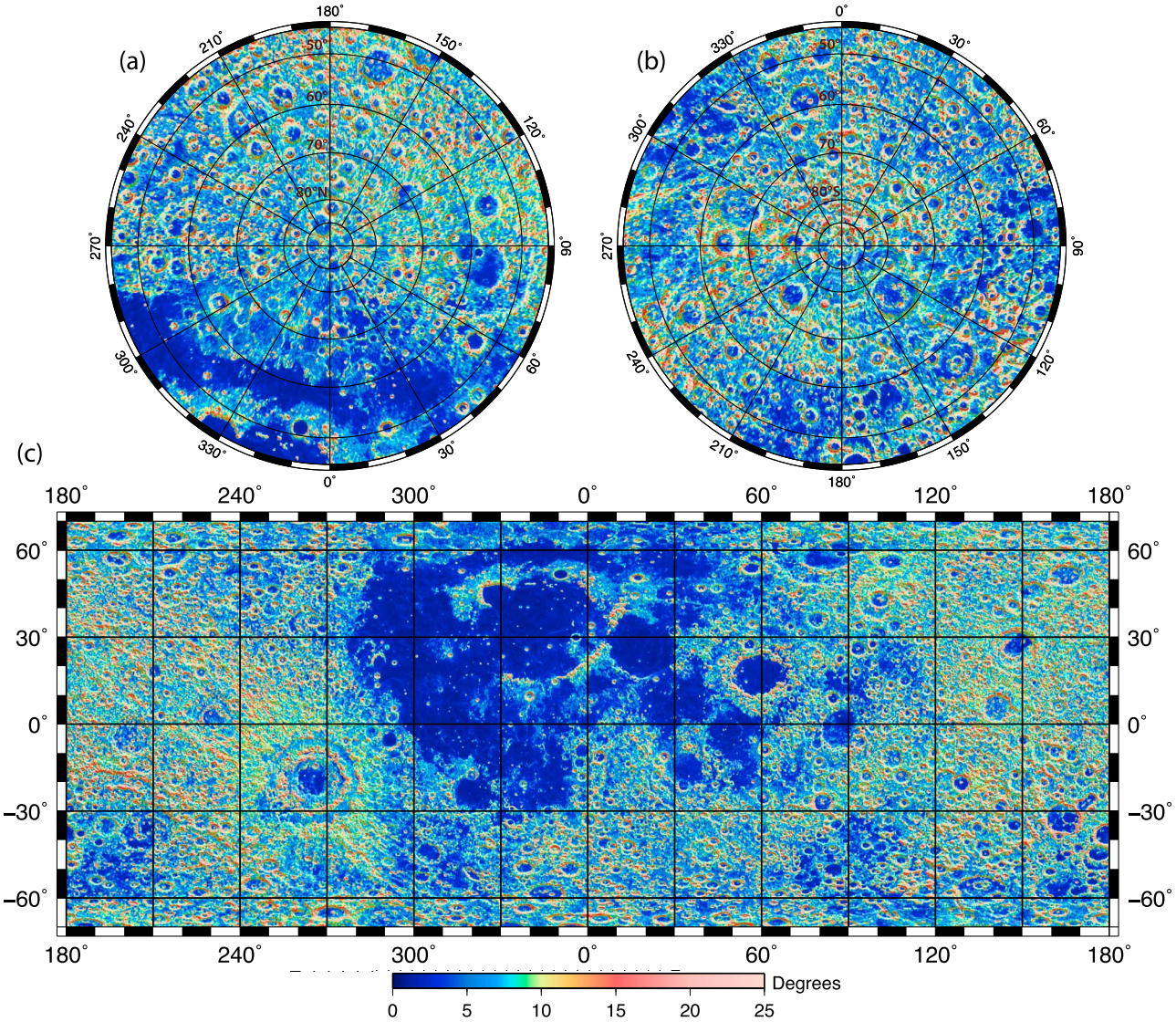

Figure 2. Median bidirectional slope map at the ~17 m effective baseline. Slopes are calculated by fitting a plane between three elevation data points. Median slopes are reported for 0.5° windows spaced 0.25° apart. (a) The north pole, shown from 45°N and (b) the south pole from 45°S, both in a stereographic projection. (c) Cylindrical equidistant projection of the latitudes from 70°S to 70°N.

before, and the median reported for 0.5° overlapping windows spaced 0.25° apart.

[9] A map of the median bidirectional slope at the ~17 m scale is shown in Figure 2. Note that while the results are reported in units of degrees, the statistics are computed in gradient units (m/m). The maria are easily distinguishable from the highlands as smooth regions with median slopes ≤3°, while the steepest median slopes (≥10°) occur within crater walls and the blocky ejecta blankets surrounding major impact basins and young rayed craters. The multiring structure of the Orientale impact basin is clearly visible in surface slopes at this scale, along with the topographically expressed secondary crater chains emerging radially from the continuous ejecta deposit. The floor of the South Pole-Aitken basin appears as a region of subdued slope; a sampling of the basin floor (excluding mare deposits, which would contribute their own roughness signature) has a median slope of 5.8°, nearly 2° lower than the median value for the highlands, 7.5°, although the distributions overlap (see Table 1). Within the nearside mare plains, large-scale flow fronts and wrinkle ridges are delineated by subtle variations in slope, particularly evident within the Imbrium, Serenetatis, and Crisium basins (Figure 3). Slopes rapidly transition between the two major highland and mare roughness units at their boundaries, where mare basalts are often tilted and deformed [e.g., *Solomon and Head*, 1980] and have only partially embayed the surrounding rougher terrain.

[10] For isotropic topography, a relationship exists between point-to-point and bidirectional slope distributions: given a one-dimensional slope distribution, the equivalent distribution of two-dimensional slopes can be found by applying a statistical correction. The probability distribution functions

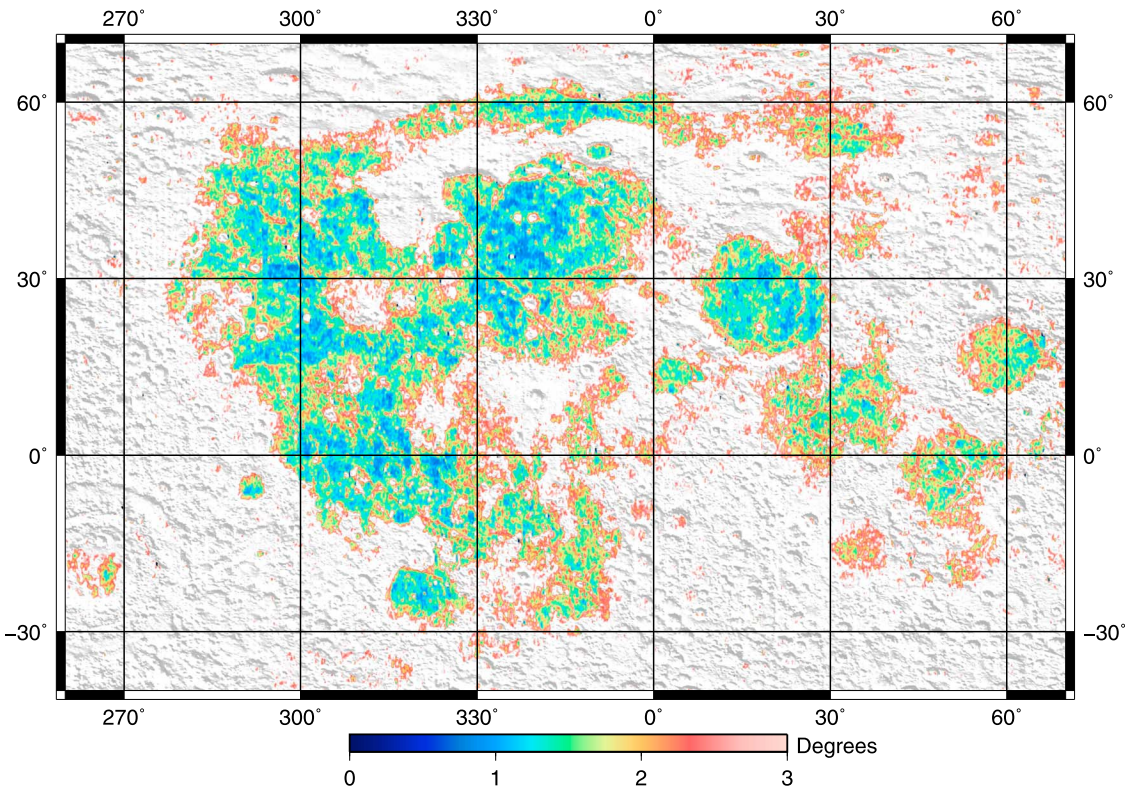

Figure 3. Median bidirectional slope, as described in Figure 2, with a color stretch designed to emphasize the subtle variations in slope within the lunar maria. Large-scale flow fronts and tectonic features such as wrinkle ridges appear as long, continuous regions of slopes higher than the surrounding plains and are most evident within the Imbrium, Crisium, and Serenetatis basins.

of the 1-D slopes, $F(p)$, and 2-D slopes, $F(s)$, are related by [*Aharonson and Schorghofer*, 2006]

$$F = \int_{|p|}^{\infty} \frac{F(s)}{\sqrt{s^2 - p^2}} ds. \tag{2}$$

In practice, this integral equation may be discretized and inverted. Figure 4 is a global comparison of our measured slopes in one and two dimensions and the adjusted point-to-point slope histogram. We find moderately good agreement between measured bidirectional slopes and those predicted from the 1-D slope distribution, although the 2-D measured slopes are slightly steeper than predicted from the 1-D distribution, typically by 25%. We can place constraints on two factors that contribute to this discrepancy. Anisotropy in our slope measurements occurs when triangles with high aspect ratios are used for plane fitting. LRO's orbital configuration creates a preferred direction for the long axis of these triangles, and because slopes are generally shallower at longer baselines, the azimuthal distribution is skewed to favor the perpendicular to the down-track direction. To minimize this effect, we included only triangles with low aspect ratios, using spots 1, 3, and 4. While some anisotropy remains, this consideration improves the agreement by nearly a factor of 2. Part of the discrepancy is also due to the fact that comparing slopes at similar baselines is rendered difficult by instrument constraints. The minimum baseline for point-to-point slopes (~25 m) is larger than the effective baseline of our preferred triangles (~17 m). As a result, bidirectional slopes have a tendency to be larger than their

Table 1. Statistical Estimators of Surface Roughness Properties for Major Lunar Geographic Regions[a]

	Highlands	Maria	South Pole-Aitken Basin: All	South Pole-Aitken Basin: Floor	South Pole	North Pole
Median slope at the ~17 m effective baseline (deg)	$7.5^{+12.3}_{-4.2}$	$2.0^{+4.1}_{-1.0}$	$7.2^{+12.0}_{-3.0}$	$5.8^{+10.5}_{-3.0}$	$7.6^{+12.4}_{-4.2}$	$6.9^{+11.5}_{-3.8}$
Median Hurst exponent	$0.95^{+0.97}_{-0.92}$	$0.76^{+0.85}_{-0.63}$	$0.95^{+0.97}_{-0.93}$	$0.94^{+0.97}_{-0.91}$	$0.95^{+0.97}_{-0.92}$	$0.94^{+0.96}_{-0.91}$
Median breakover scale (km)	$0.98^{+1.13}_{-0.74}$	$0.53^{+0.97}_{-0.24}$	$1.01^{+1.14}_{-0.81}$	$1.01^{+1.15}_{-0.82}$	$1.01^{+1.15}_{-0.79}$	$0.97^{+1.12}_{-0.73}$
Typical deviogram shape(s)	Monofractal, bilinear	Complex	Monofractal, bilinear	Monofractal, bilinear, complex	Monofractal, bilinear	Monofractal, bilinear, complex

[a]The median value is reported along with the 25% and 75% percentile points as a measure of the width of each distribution.

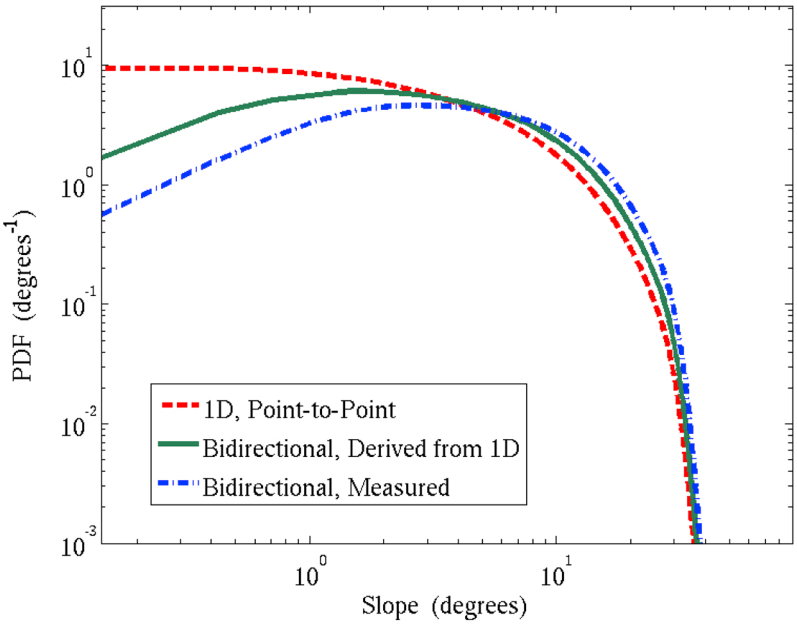

Figure 4. Global slope histograms for the Moon. The red (dashed) line shows the distribution of measured point-to-point slopes at the 25 m baseline. This distribution is recalculated to the green (solid) line using the method of *Aharonson and Schorghofer* [2006] to predict bidirectional slopes from the one-dimensional slope histogram. Measured bidirectional slopes at the ~17 m scale are shown in blue (dot-dashed line). All distributions are normalized such that the integral of the probability density function is equal to 1. Assuming that the topography is indeed isotropic, the remaining discrepancy in the measured and derived distributions is due to the geometry of the triangles used to measure 2-D slopes and to the mismatch in scales over which the slopes are measured in each case. Both effects are constrained by LRO's orbital configuration and instrument limitations.

1-D counterparts, where a component of this difference is due solely to the mismatch in baselines. A slightly better agreement can be obtained by using a local Hurst exponent (defined in section 3.3) to scale the slope distribution to a common horizontal baseline. However, this demands additional assumptions and the improvement is not large.

3.2. Median Differential Slope

[11] The median differential slope is a measure introduced by *Kreslavsky and Head* [2000] to disentangle small- and large-scale contributions to surface roughness. For the baseline of interest, L, it isolates roughness features on the order of L by subtracting the point-to-point slope at twice the given baseline:

$$s_d = \frac{z_{\frac{L}{2}} - z_{-\frac{L}{2}}}{L} - \frac{z_L - z_{-L}}{2L}. \quad (3)$$

The resulting value, s_d, is a measure of slopes at a certain scale with respect to longer-wavelength features.

[12] As with the RMS and median bidirectional slopes, median differential slopes were calculated in 0.5° windows spaced 0.25° apart, and only those windows with more than 250 measurements were retained. Following the work of *Kreslavsky and Head* [2000], differential slopes at a given baseline were calculated according to (3) by subtracting slopes calculated at two different baselines. Practically, this involves calculating the position of each slope midpoint along the track length and interpolating the slope midpoints at the longer baseline to the points occupied by the smaller-baseline slope profile to accomplish the subtraction at the correct location. This method ensures that the two slope profiles are always aligned correctly, thereby avoiding errors in the value of the differential slope calculated. This procedure is identical to the detrending process described in section 3.3 and illustrated in Figure 6, except that the ratio of baselines is always 2.

[13] Differential slopes were calculated in this manner for all baselines ranging from one shot spacing apart (~57 m) to 25 shot spacings apart (~1.4 km). Only profiles involving a single laser spot were considered for the calculation, so that the slopes over multiple baselines would be computed along the same direction. Figure 5 shows a composite color map of the lunar surface which presents roughness at three different scales, ~560 m (10 shot spacings) in the red channel, ~220 m (4 shot spacings) in green, and ~57 m (1 shot spacing) in blue. Variations in the roughness properties across the surface are apparent and substantial, showing intriguing characteristic signatures for several terrain types. The lunar maria are roughest at the smallest scale and smoother at large scales, making them easily distinguishable by their blue tones in the composite image. A comparison of mare ages [*Hiesinger et al.*, 2010] with Figure 5 shows that flows of different ages have different roughness signatures; the youngest (e.g., those within Oceanus Procellarum and

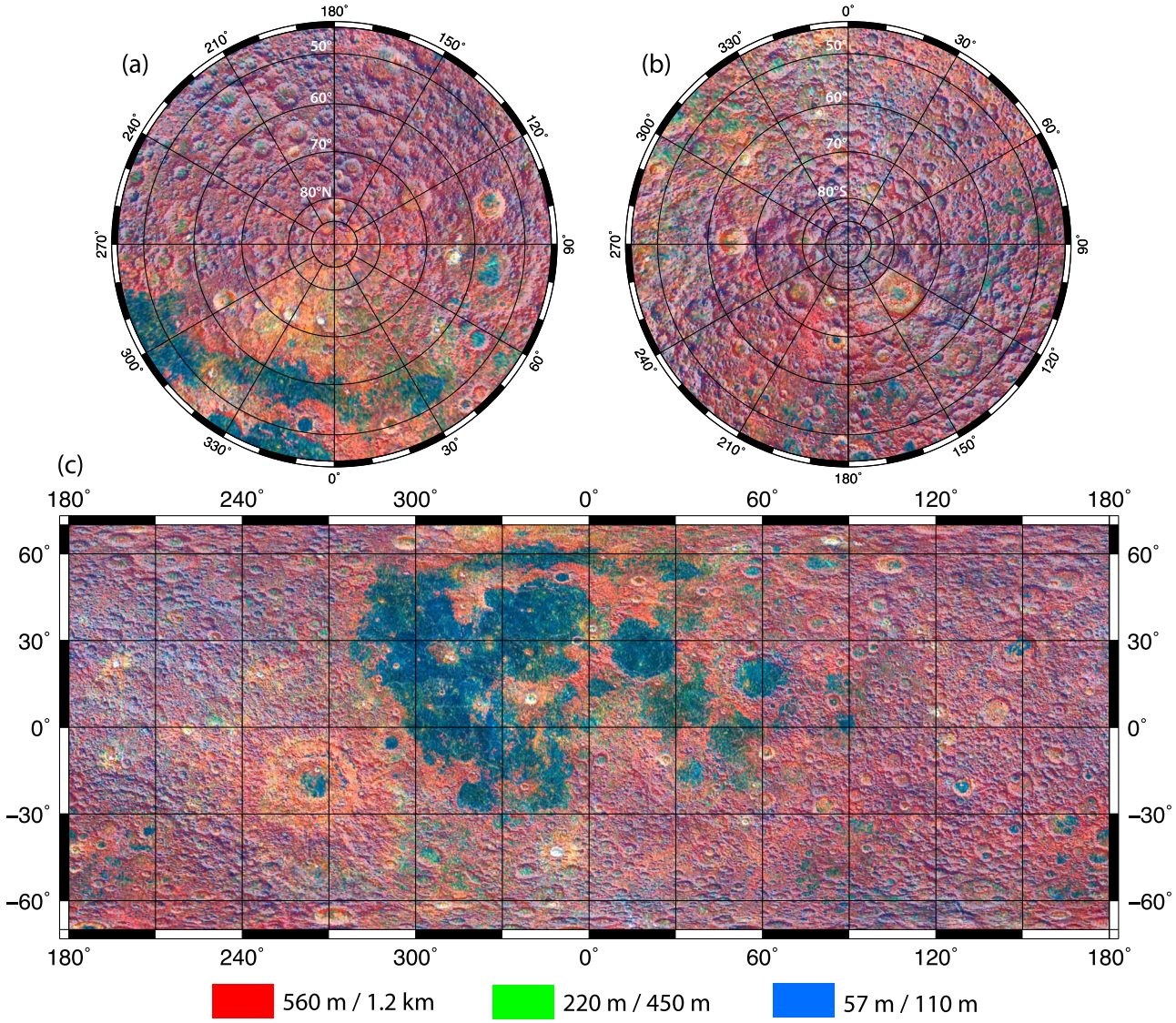

Figure 5. Composite color map of median differential slope. Differential slopes at three different baselines were calculated according to (2). The blue channel corresponds to roughness at the smallest scale considered, one shot spacing, or ~57 m. Green represents roughness at the ~220 m baseline, and red the ~560 m baseline. Map projections are the same as in Figure 2.

Mare Imbrium) are rough only at the smallest scale, while successively older flows (e.g., Mare Tranquilitatis and Mare Marginis) increase in roughness at larger scales. At the smallest scale, roughness remains approximately constant with age, potentially indicating that saturation on small scales occurs on relatively short timescales. In the composite map, these age variations correspond to a transition in color from deep blue to blue-green. The ejecta surrounding major basins (particularly around Orientale, but also older basins) are roughest at the longest scale, causing these regions to appear orange or red. Young, Copernican-age craters appear white because they are bright in all channels; the least modified features on the Moon, they are rough at all scales. Moreover, the ray systems related to these craters, so evident in albedo maps but not obviously expressed as topographic relief, are roughest at the intermediate scale, probably reflecting crater chains and clusters that often populate crater rays [e.g., *Oberbeck*, 1975; *Pieters et al.*, 1985]. As a result, they are clearly expressed as star-shaped yellow to orange halos surrounding each feature (Figure 6). Other, subtler variations, not obviously related to a single geologic feature, occur across much of the surface. The region spanning latitudes 30°S to 60°N and longitudes 160°E to 240°E, representing a large uninterrupted stretch of lunar highlands, appears relatively bright and with a mottled appearance, consistent with an old surface saturated with craters at many different scales. The South Pole-Aitken basin is somewhat redder than its surroundings, except for the patches of mare within superimposed craters.

[14] As a diagnostic tool for distinguishing unique roughness units, the median differential slope is a useful measure of surface roughness. However, because it involves measur-

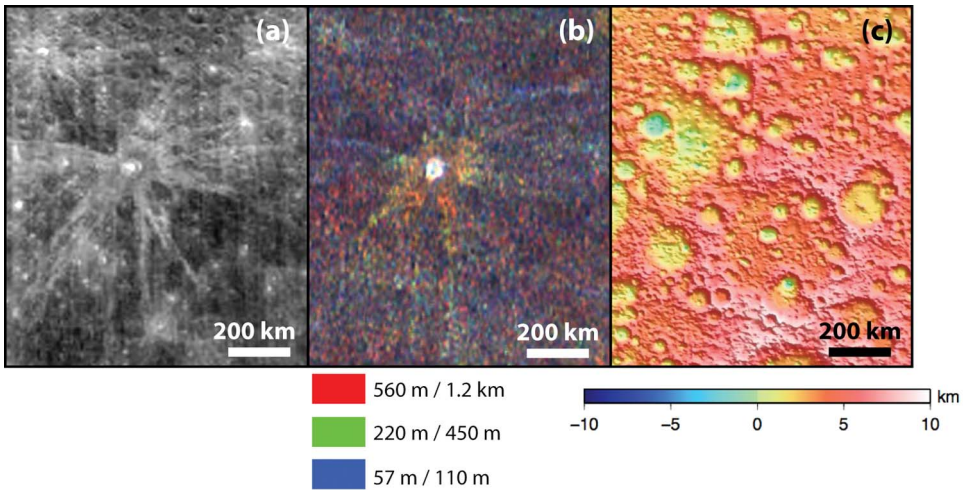

Figure 6. Lunar far-side crater Jackson and its ray system, centered at 19°E and 22.4°N, shown in (a) the 750 nm Clementine albedo map [e.g., *McEwen and Robinson*, 1997], (b) the median differential slope map, as in Figure 5, and (c) the topography [*Smith et al.*, 2010b]. Rays of young, Copernican-age craters are clearly expressed as streaks of high albedo relative to the background. Though they do not add obvious relief to the topography, the rays are distinctly rougher at the ~220 m and ~560 m baselines compared to the highlands, making them appear yellow to orange in the composite roughness map.

ing small-scale roughness with respect to long-wavelength roughness features, it can be more difficult to interpret physically as a slope characteristic. For this reason, the median absolute slope at a given scale is a more intuitive parameter.

3.3. Hurst Exponent

[15] Topography is often considered a nonstationary random field with self-affine fractal-like properties [*Turcotte*, 1997]. Self-affinity implies a scaling behavior such that an increase of factor r in the horizontal length scale corresponds to an increase in the vertical length scale of r^H, where H is known as the Hurst exponent and falls between 0 and 1 for real surfaces [e.g., *Turcotte*, 1997; *Orosei et al.*, 2003]. The Hurst exponent is directly related to both the fractal dimension of the surface, $D = 1 + d - H$, and the slope of the power spectrum, $\beta = 2H + d$, where in each case d is the number of spatial dimensions: 1 for a profile or 2 for a surface [*Schroeder*, 1991].

[16] The Hurst exponent describes the power law behavior of surface slopes when they are scaled to different horizontal baselines:

$$s(\Delta x) = s_0 \left(\frac{\Delta x}{\Delta x_0}\right)^{H-1} = \frac{\nu(\Delta x)}{\Delta x}. \tag{4}$$

Written as such, it is clear that the deviation $\nu(\Delta x) \propto (\Delta x)^H$. H can thus be estimated as the slope of a best-fit line to $log[\nu(\Delta x)]$ versus $log(\Delta x)$ [*Orosei et al.*, 2003].

[17] We calculate the RMS deviation for a range of baselines from ~57 m to ~2.7 km (1 to 50 shot spacings) and analyze the deviogram, or structure function, $\nu(\Delta x)$. As in the previous calculations, the deviation values were calculated along track in overlapping windows. However, *Shepard et al.* [2001] showed that errors can be introduced when the range over which the Hurst exponent is fit exceeds 10% of the topographic profile length (the window size).

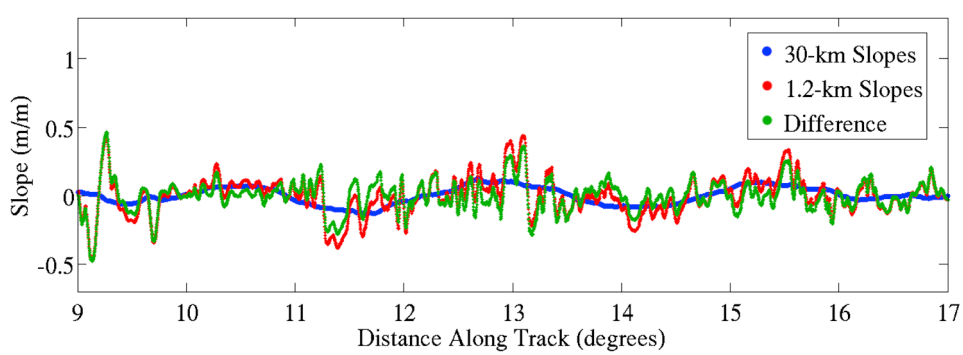

Figure 7. Method of detrending slope data. Slopes measured at the ~30 km baseline (in blue) are subtracted from ~1.2 km slopes (red), leaving a detrended slope profile behind (green) and avoiding large-scale tilts in the topography.

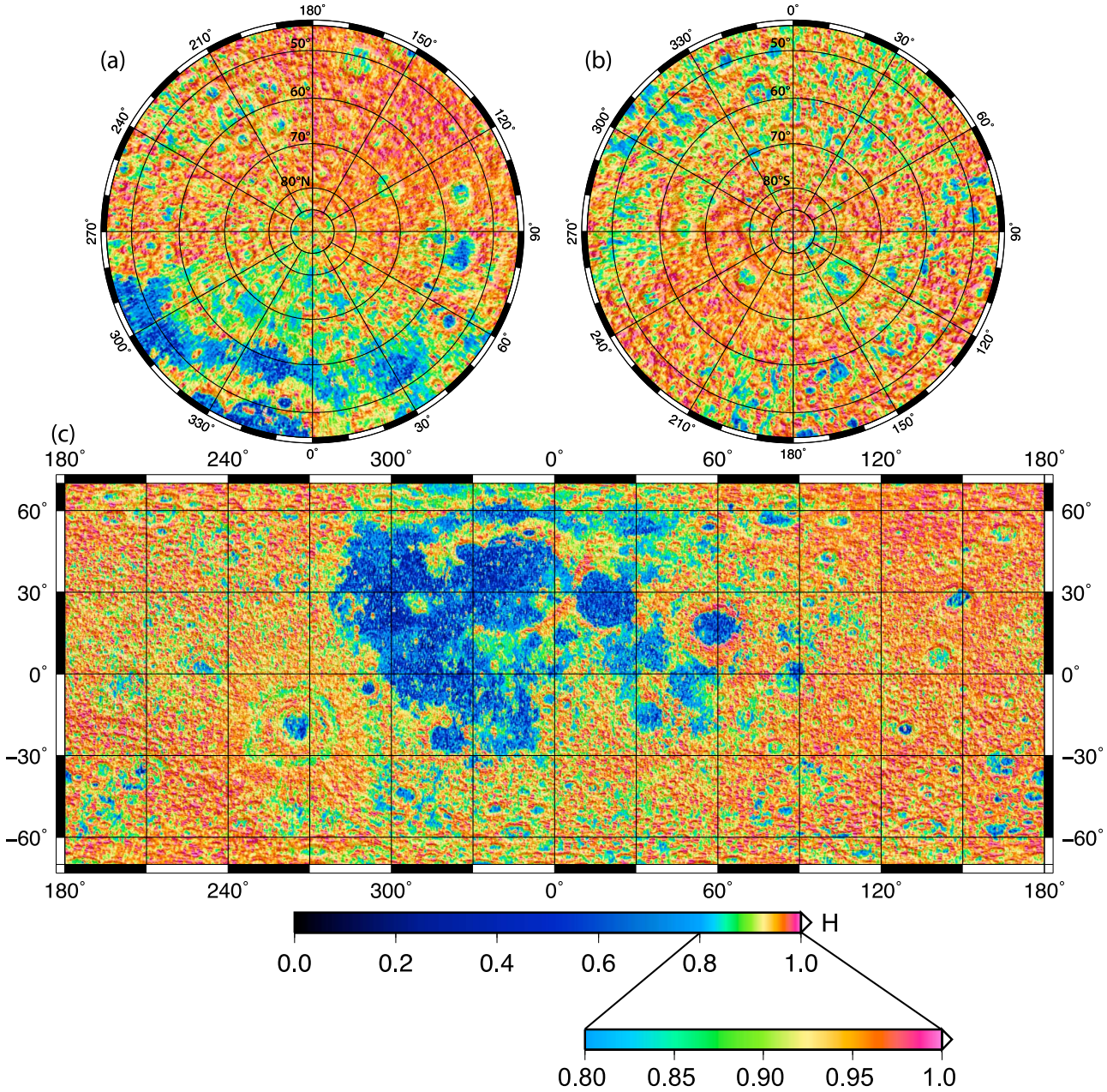

Figure 8. Hurst exponent map. For each 0.5° pixel, the Hurst exponent is computed as the slope of the best fit line to the deviogram, over the baseline range beginning at one shot spacing (~57 m) and extending to the breakover point for that location, Δx_0. The color scale was chosen to emphasize the dynamic range of the variations from 0.8 to 1, although substantially smaller H is common in the maria. Map projections are the same as in Figure 2.

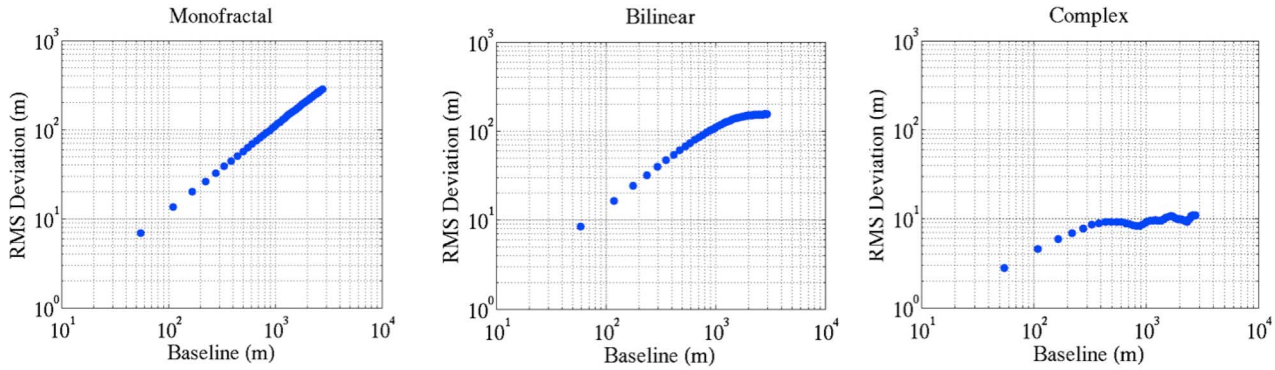

Figure 9. Observed deviogram shapes. Though many deviograms are monofractal over the baseline range explored (from 1 to 50 shot spacings, or ~57 m to ~2.7 km), most are bilinear, breaking over to a shallower slope at a certain breakover baseline. Many others exhibit complex behavior that is not well characterized by a line over a given portion of the baseline range.

Therefore, we use 1° (30 km) windows for this calculation, spaced 0.5° (15 km) apart. We use only shot-to-shot profiles of laser spot 3, selected for its consistency.

[18] To remove roughness features on the order of our window size, we detrend each deviogram at the 30 km scale. This process deemphasizes large-scale roughness features in favor of small-scale features of more interest to this study, and it avoids biases due to long-wavelength trends that are undersampled within each window [*Shepard et al.*, 2001]. Figure 7 shows how the detrending is accomplished. Slopes measured at the 30 km baseline are subtracted from small-scale slopes, leaving a slope profile with a mean near zero within the window. Slopes at scales less than 3 km are only slightly affected by the detrending process, except where long-wavelength slopes are high, for example, those near mountain ranges.

[19] In some cases, the deviograms are well characterized by a single log-log slope (exponent), but many others transition to a different slope at a certain length scale. This behavior is well documented in the literature for other planetary surfaces [e.g., *Shepard et al.*, 2001; *Morris et al.*, 2008] and is often attributed to surface processes acting at small and large scales. For the Hurst exponent fit within each window along the track, we use baselines ranging from one shot spacing (~57 m) to the breakover scale (the point where the deviogram diverges from a straight line, Δx_0) for that location. Figure 8 is a map of the Hurst exponent calculated in this way. Although the baseline range used in this map varies over the surface, this method avoids including fits to nonlinear sections of each deviogram and thus presents a more accurate estimate of the Hurst exponent at the smallest available scales.

[20] The highest Hurst exponents on the Moon are found in the highlands within crater walls and the rims and ejecta of large basins, and in these regions values above 0.95 are not uncommon. This result is surprising, given that typical Hurst exponents for topographic surfaces on the Earth and Mars are lower, between 0.7 and 0.9 [*Kreslavsky and Head*, 2000; *Orosei et al.*, 2003; *Morris et al.*, 2008]. A Hurst exponent of 1 implies self-similar topography, meaning the roughness at small scales is exactly replicated at large scales. The high values observed for the lunar highlands may be related to the density of impact craters in these regions and the absence of competing morphologic processes to transport fine material downhill. Hurst exponents within the lunar maria are lower than those within the highlands, with a median value of 0.76, indicating smoother topography at large scales relative to small scales.

[21] To classify deviogram shapes, we use a method similar to that of *Main et al.* [1999] that establishes whether a given deviogram is best fit by one line or by two, or whether

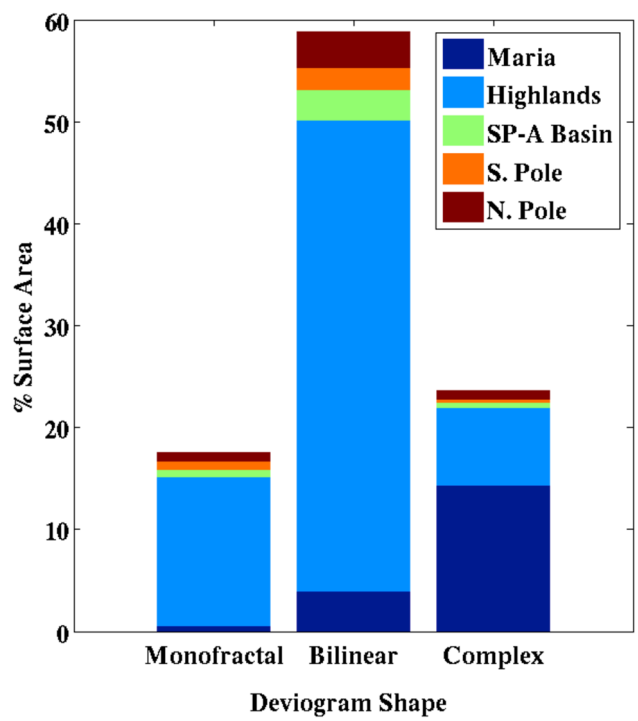

Figure 10. Abundance of deviogram shapes by surface area, sorted by region. The most common deviogram shape is bilinear (~59%), with monofractal (~17%) and complex (~24%) making up the remaining area. The highlands are almost entirely bilinear and monofractal, while the maria contain primarily complex deviograms.

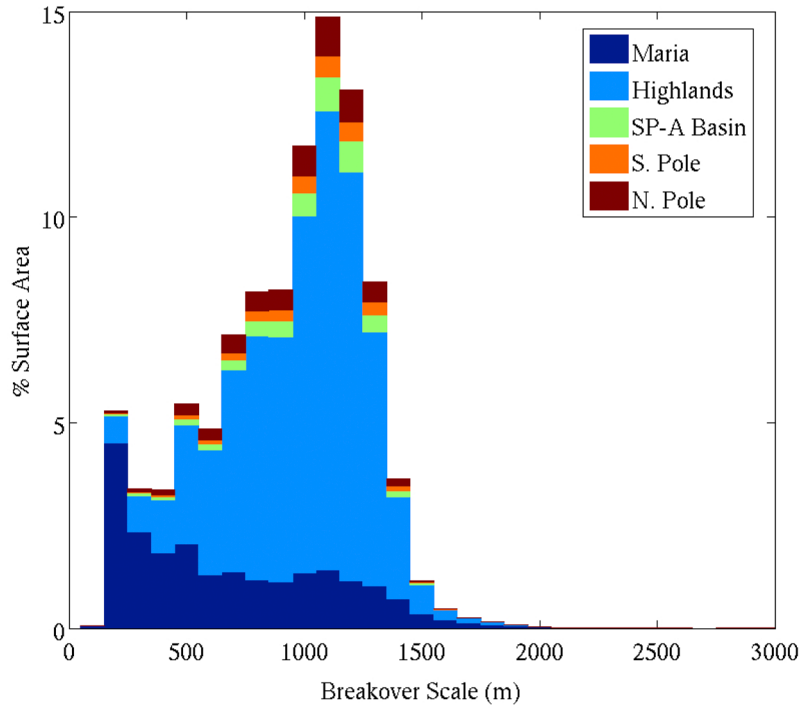

Figure 11. Breakover point histogram, sorted by region. Whereas the maria exhibit a broad range of breakover points, reflecting the complexity of deviograms in these regions, the other regions have a strongly peaked distribution of breakover points near 1 km. This characteristic baseline indicates a transition between two surface processes and may tell us about the Moon's surface history.

the deviogram is poorly fit by any linear model. We compute the least squares fits in each case and compare the sums of the residuals, adding a penalty when additional parameters are introduced into the fit (i.e., three parameters are required for a line, five for two lines). This method classifies each deviogram by its shape (Figure 9) and yields the relevant slope(s) of the deviogram, an estimate of the breakover baseline, Δx_0, and confidence intervals on all of the above.

[22] Figure 10 shows the distribution of deviogram shapes across the surface of the Moon and how they partition among major topographic regions. Polygons defining the lunar maria were taken from the U.S. Geological Survey series of geologic maps of the Moon [*Wilhelms and McCauley*, 1971; *Wilhelms and El-Baz*, 1977; *Scott et al.*, 1977; *Lucchitta*, 1977; *Stuart-Alexander*, 1978; *Wilhelms et al.*, 1979] and used to select data within the mare plains. The rim of the South Pole-Aitken basin was defined using the best-fit ellipse from the work of *Garrick-Bethell and Zuber* [2009]. The polar regions included latitudes from 60° to the pole, excluding patches of mare basalts and the South Pole-Aitken basin region. All areas falling outside these regions were designated highlands. By surface area, most deviograms are best characterized by two lines (~59%), with the remainder of the surface nearly evenly divided between monofractal (~17%) and complex (~24%) deviogram shapes, in which the slope changes continuously and rapidly with baseline, often alternating sign. Complex deviograms are mainly found in the lunar maria, whereas the highlands exhibit primarily monofractal or bifractal behavior. Other geographic regions, including the north and south poles and the South Pole-Aitken basin, behave much like the lunar highlands. This partitioning indicates a profound difference in character between the two major units; on the one hand, highland deviograms behave as nearly self-similar fractals, whereas mare topography diverges from fractal behavior altogether at the breakover point.

[23] Within areas that adhere to fractal behavior, the baseline at which the breakover occurs, Δx_0, is a significant parameter constrained by the two-line fit to the deviogram because it has a physical meaning related to the surface processes that contribute to the evolution of the Moon's topography. Formation and modification mechanisms act over a range of scales and may have distinct Hurst exponents. The breakover point is thus an estimate of the scale at which surface processes acting at longer scales are overtaken by those acting on smaller scales. In other words, it represents the baseline at which competing surface processes are equal contributors to the topography.

[24] Figure 11 is a stacked histogram showing the distribution of breakover points for all deviograms and their locations within the major geographic regions. Within the maria, breakover points are broadly distributed, reflecting the complex nature of the deviograms found there. All other regions, however, have a strong peak at ~1 km, suggesting a significant transition between surface processes acting above and below this scale. Impact cratering and mare basalt emplacement are most likely responsible for many of the key differences between the lunar highlands and the maria. Other processes that may have contributed to the observed

roughness properties remain to be identified and quantified, but likely candidates for exploration include mass wasting, perhaps due to seismic shaking, ejecta mantling, and micrometeorite gardening.

4. Conclusions

[25] New altimetry data from LOLA allow a unique opportunity to quantify the surface roughness properties of the Moon. We find that topography within the highlands and the mare plains exhibits substantially different behaviors, while other geographic regions show more subtle variations. Table 1 presents a summary of the most important roughness characteristics for each major region. For each parameter, the median is reported, as it best reflects a typical value for the region, along with the 25% and 75% percentile points, which indicate the shoulders of each distribution and hence provide an estimate of the width. We find that most of the surface is characterized by fractal-like behavior with either one or two Hurst exponents over the baseline range covered, from ~57 m to ~2.7 km, with a strong tendency to break over near the 1 km scale. The Hurst exponent is generally high in the lunar highlands, reflecting nearly self-similar topography in these regions. Within the maria, however, deviograms transition from fractal at small scales to complex at a range of breakover points, and the Hurst exponent is both lower and more diverse.

[26] **Acknowledgments.** The authors would like to acknowledge the LRO and LOLA engineering teams, without whom the data presented here would not have been possible. The research was partially funded by NASA grants NNX08AZ54G and NNG09EK06C:1.

References

Aharonson, O., and N. Schorghofer (2006), Subsurface ice on Mars with rough topography, *J. Geophys. Res.*, *111*, E11007, doi:10.1029/2005JE002636.

Aharonson, O., M. T. Zuber, and D. H. Rothman (2001), Statistics of Mars' topography from the Mars Orbiter Laser Altimeter: Slopes, correlations, and physical models, *J. Geophys. Res.*, *106*, 23,723–23,736, doi:10.1029/2000JE001403.

Daniels, F. B. (1963), Radar determination of the root mean square slope of the lunar surface, *J. Geophys. Res.*, *68*, 449–453, doi:10.1029/JZ068i002p00449.

Garrick-Bethell, I., and M. T. Zuber (2009), Elliptical structure of the lunar South Pole-Aitken basin, *Icarus*, *204*, 399–408, doi:10.1016/j.icarus.2009.05.032.

Hiesinger, H., J. W. Head, U. Wolf, R. Jaumann, and G. Neukum (2010), Ages and stratigraphy of lunar mare basalts in Mare Frigoris and other nearside maria based on crater size-frequency distribution measurements, *J. Geophys. Res.*, *115*, E03003, doi:10.1029/2009JE003380.

Kreslavsky, M. A., and J. W. Head (2000), Kilometer-scale roughness of Mars: Results from MOLA data analysis, *J. Geophys. Res.*, *105*, 26,695–26,712, doi:10.1029/2000JE001259.

Lucchitta, B. K. (1977), Geologic map of the north side of the Moon, *U.S. Geol. Surv. Misc. Invest. Map, I-1062*, scale 1:5,000,000.

Main, I. G., T. Leonard, O. Papasouliotis, C. G. Hatton, and P. G. Meredith (1999), One slope or two? Detecting statistically significant breaks of slope in geophysical data, with application to fracture scaling relationships, *Geophys. Res. Lett.*, *26*, 2801–2804, doi:10.1029/1999GL005372.

McEwen, A. S., and M. S. Robinson (1997), Mapping of the moon by Clementine, *Adv. Space Res.*, *19*, 1523–1533, doi:10.1016/S0273-1177(97)00365-7.

Moore, H. J., and G. L. Tyler (Eds.) (1973), *Apollo 17: Preliminary science report*, *NASA SP-330*.

Morris, A. R., F. S. Anderson, P. J. Mouginis-Mark, A. F. C. Haldemann, B. A. Brooks, and J. Foster (2008), Roughness of Hawaiian volcanic terrains, *J. Geophys. Res.*, *113*, E12007, doi:10.1029/2008JE003079.

Neumann, G. A., and D. W. Forsyth (1995), High resolution statistical estimation of seafloor morphology: Oblique and orthogonal fabric on the flanks of the Mid-Atlantic Ridge, 34°–35.5°S, *Mar. Geophys. Res.*, *17*, 221–250, doi:10.1007/BF01203464.

Oberbeck, V. R. (1975), The role of ballistic erosion and sedimentation in lunar stratigraphy, *Rev. Geophys.*, *13*, 337–362.

Orosei, R., R. Bianchi, A. Coradini, S. Espinasse, C. Federico, A. Ferriccioni, and A. I. Gavrishin (2003), Self-affine behavior of Martian topography at kilometer scale from Mars Orbiter Laser Altimeter data, *J. Geophys. Res.*, *108*(E4), 8023, doi:10.1029/2002JE001883.

Pieters, C. M., J. B. Adams, M. O. Smith, P. J. Mouginis-Mark, and S. H. Zisk (1985), The nature of crater rays: The Copernicus example, *J. Geophys. Res.*, *90*, 12,393–12,413, doi:10.1029/JB090iB14p12393.

Schroeder, M. (1991), *Fractals, Chaos, and Power Laws: Minutes From an Infinite Paradise*, 1st ed., 429 pp., W. H. Freeman, New York.

Scott, D. H., J. F. McCauley, and M. N. West (1977), Geologic map of the west side of the Moon, *U.S. Geol. Surv. Misc. Invest. Map, I-1034*, scale 1:5,000,000.

Sharpton, V. L., and J. W. Head (1985), Analysis of regional slope characteristics on Venus and Earth, *J. Geophys. Res.*, *90*, 3733–3740, doi:10.1029/JB090iB05p03733.

Shepard, M. K., B. A. Campbell, M. H. Bulmer, T. G. Farr, L. R. Gaddis, and J. J. Plaut (2001), The roughness of natural terrain: A planetary and remote sensing perspective, *J. Geophys. Res.*, *106*, 32,777–32,796, doi:10.1029/2000JE001429.

Smith, D. E., et al. (2001), Mars Orbiter Laser Altimeter: Experiment summary after the first year of global mapping of Mars, *J. Geophys. Res.*, *106*, 23,689–23,722, doi:10.1029/2000JE001364.

Smith, D. E., et al. (2010a), The Lunar Orbiter Laser Altimeter investigation on the Lunar Reconnaissance Orbiter Mission, *Space Sci. Rev.*, *150*, 209–241, doi:10.1007/s11214-009-9512-y.

Smith, D. E., et al. (2010b), Initial observations from the Lunar Orbiter Laser Altimeter (LOLA), *Geophys. Res. Lett.*, *37*, L18204, doi:10.1029/2010GL043751.

Smith, D. K., and T. H. Jordan (1988), Seamount statistics in the Pacific Ocean, *J. Geophys. Res.*, *93*, 2899–2918, doi:10.1029/JB093iB04p02899.

Solomon, S. C., and J. W. Head (1980), Lunar mascon basins: Lava filling, tectonics, and evolution of the lithosphere, *Rev. Geophys.*, *18*, 107–141.

Stuart-Alexander, D. E. (1978), Geologic map of the central far side of the Moon, *U.S. Geol. Surv. Misc. Invest. Map, I-1047*, scale 1:5,000,000.

Turcotte, D. L. (1997), *Fractals and Chaos in Geology and Geophysics*, 2nd ed., 398 pp., Cambridge Univ. Press, Cambridge, U. K.

Wilhelms, D. E., and F. El-Baz (1977), Geologic map of the near side of the Moon, *U.S. Geol. Surv. Misc. Invest. Map, I-703*, scale 1:5,000,000.

Wilhelms, D. E., and J. F. McCauley (1971), Geologic map of the east side of the Moon, *U.S. Geol. Surv. Misc. Invest. Map, I-948*, scale 1:5,000,000.

Wilhelms, D. E., K. A. Howard, and H. G. Wilshire (1979), Geologic map of the south side of the Moon, *U.S. Geol. Surv. Misc. Invest. Map, I-1162*, scale 1:5,000,000.

Yokota, Y., et al. (2008), Mapping of lunar topographic roughness by digital terrain model, *Lunar Planet. Sci.*, *XXXIX*, Abstract 1921.

Zuber, M. T., et al. (2010), The Lunar Reconnaissance Orbiter Laser Ranging investigation, *Space Sci. Rev.*, *150*, 63–80, doi:10.1007/s11214-009-9511-z.

O. Aharonson and M. A. Rosenburg, Division of Geological and Planetary Sciences, MC 150-21, California Institute of Technology, Pasadena, CA 91125, USA. (megr@gps.caltech.edu)

J. W. Head, Department of Geological Sciences, Brown University, Providence, RI 02912, USA.

M. A. Kreslavsky, Department of Earth and Planetary Sciences, University of California, Santa Cruz, CA 95064, USA.

E. Mazarico, G. A. Neumann, D. E. Smith, and M. T. Zuber, Department of Earth, Atmospheric, and Planetary Science, Massachusetts Institute of Technology, Cambridge, MA 02139, USA.

M. H. Torrence, NASA Goddard Space Flight Center, Greenbelt, MD 20770, USA.